Two-dimensional spectroscopic imaging of individual ferromagnetic nanostripes

Han-Jong Chia,[1,2,*] Feng Guo,[1,2] L. M. Belova,[3] and R. D. McMichael[1,†]

[1]*Center for Nanoscale Science and Technology, National Institute of Standards and Technology, Gaithersburg, Maryland 20899, USA*
[2]*Maryland Nanocenter, University of Maryland, College Park, Maryland 20742, USA*
[3]*Department of Materials Science and Engineering, Royal Institute of Technology, 10044 Stockholm, Sweden*

We use ferromagnetic-resonance force microscopy to spectroscopically image the edge modes in individual 700 nm and 400 nm wide Permalloy stripes with a spatial resolution on the order of 200 nm. The imaging clearly identifies some resonances as edge modes in stripes in a case where mode identification by comparison with micromagnetic modeling is not clear. Combined spectroscopic and spatial scans reveal clear differences in the edge mode resonances at opposite edges of the stripes as well as inhomogeneity along the length of the stripe.

PACS number(s): 75.78.−n, 75.30.Ds, 75.70.Ak

I. INTRODUCTION

The development of future spintronic devices such as racetrack memory,[1] domain-wall logic,[2] and spin torque magnetic random access memory[3] is in part dependent upon the ability to characterize defects. In order to better understand the sources of defects and their effects on magnetization dynamics there is a need to develop suitable defect measurement techniques, especially those that are capable of resolving individual devices or even features within the devices.

One particular area of interest concerns the magnetic properties of film edges in magnetic nanostructures since they are known to play a role in the magnetic behavior of the entire nanostructure. A simple geometric argument suggests that the edge properties become increasingly important as devices are made smaller. Several methods have been developed to detect localized magnetic precession modes that can form at film edges based on ferromagnetic resonance (FMR),[4,5] including Brillouin light-scattering spectroscopy (BLS),[6,7] and time resolved Kerr microscopy.[8–10]

The edge modes feature maximum precession amplitude at the film edge, and they are consequently sensitive to magnetic properties at the edge. For applied fields sufficient to saturate the magnetization perpendicular to the edge, the effects of film edge properties on edge mode resonance have been explored theoretically[11] and experimentally for effects including film thickness,[12] edge oxidation,[13] interactions at edges of trilayer films,[14] and possibly most importantly for this paper the effects of sidewall angle and edge profile.[4,15] From the previous studies, deviations from vertical, smooth, clean film edge surfaces generally result in reductions in the edge mode resonance field for a given excitation frequency.

With the exception of time resolved Kerr measurements[8,9] and thermal imaging,[16] many of the edge mode spectroscopy results reported to date have been measured on arrays of stripes using FMR or BLS methods that do not provide spatial images of the precession pattern. In these measurements, comparison with micromagnetic modeling or other theory has proven helpful in identifying the "bulk" modes and the edge modes. However, the accuracy of these models and the accuracy of the mode identification both depend heavily on knowledge of materials properties and geometry, and these properties are not always well known, especially at the film edges. Mode identification may be further complicated by the presence of

higher-order edge modes that form in the low-field region near the film edge.[7]

In this paper we demonstrate one-dimensional (1D) and two-dimensional (2D) imaging and spectroscopy of the center and edge modes of ferromagnetic nanostripes using ferromagnetic-resonance force microscopy (FMRFM) with a spatial resolution on the order of 200 nm and clear identification of edge modes. The FMRFM measurement and modeling methods are described in Sec. II. Section III includes results and discussion of spectroscopic measurements in Sec. III A, imaging in Sec. III B, and image length scales in Sec. III C.

II. METHODS

Ferromagnetic-resonance force microscopy is a variant of FMR where the magnetization precession is detected by magnetic forces on a small magnetic tip mounted on a microcantilever [Fig. 1(a)].[17–19] The magnetic cantilever tip is brought within a few hundred nanometers of the sample, which is excited by microwave-frequency magnetic fields, driving the sample spins into precession. Because the modulus of the magnetization vector is very nearly conserved, the precession is accompanied by a decrease in the static magnetization, a decrease that is proportional to the energy stored in the excited mode.[18] The change in the sample magnetization changes the magnetic forces between the tip and sample, and it results in a detectable change in the cantilever oscillation.

The spatial resolution of FMRFM methods may depend on a number of geometrical factors including the tip geometry and tip height.[18] Magnetic factors, such as the stray field from the tip, may be equally important. A weak tip field may simply perturb the resonance field of the sample,[18] or in the opposite limit of strong tip fields precession may be either suppressed[20] or localized by the tip field.[21–25] For a strongly localized precession mode in a normally magnetized film, Lee *et al.* recently demonstrated imaging of material inhomogeneity with a resolution of 200 nm as the tip and accompanying localized mode were scanned.[23] Later micromagnetic calculations predicted a resolution of 280 nm for the parameters of Lee *et al.*, and also predicted resolution as low as 95 nm for fields applied in plane.[25]

The experimental details of our setup include a silicon cantilever with a resonance frequency of 8.1 kHz and a nominal spring constant of 0.1 N/m. The magnetic tip, with a nominal
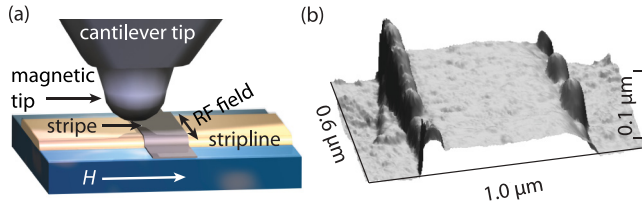
FIG. 1. (Color online) (a) Schematic setup for FMRFM. A soft magnetic tip on a cantilever is placed just above the stripe sitting on the center stripe of a coplanar waveguide. (b) AFM topographical scan of a stripe (width 700 nm) showing asymmetry of the edges.
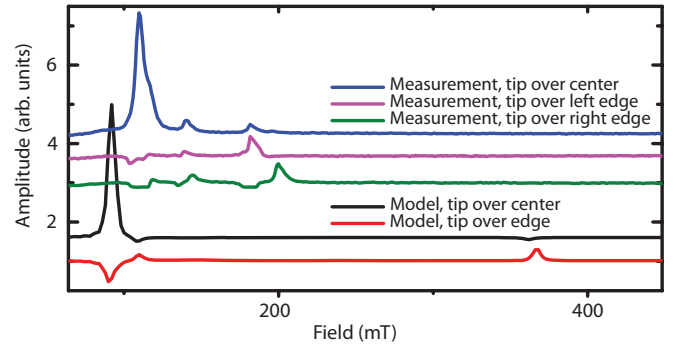

FIG. 2. (Color online) Measured and modeled FMRFM spectra for tip positions at the center and edges of the 700 nm stripe. The strong, low-field resonances are labeled as center modes and the high-field resonances are labeled as edge modes.

diameter of 500 nm, was deposited on the cantilever using electron-beam induced deposition.[26] The composition of the tip obtained through energy-dispersive x-ray spectroscopy is 73.7% cobalt, 16.9% oxygen, and 9.4% carbon with a standard deviation uncertainty of 1%. Microwave excitation is delivered by a coplanar waveguide with center and ground lines (line widths and gaps, all 2 μm) that are composed of Cr (5 nm) / Au (150 nm). An Al_2O_3 layer (thickness 25 nm) was deposited on top of the waveguide using atomic layer deposition to electrically insulate it from the stripes.

While spintronic devices are typically fabricated with multilayer structures that may show interesting interlayer effects,[14] for simplicity here we use a single layer of Permalloy. The stripes were defined using electron-beam lithography with widths of 400 nm and 700 nm followed by electron-beam deposition of a trilayer structure, [Ta (5 nm) / $Ni_{80}Fe_{20}$ (25 nm) / Ta (5 nm)] and patterning by liftoff. The liftoff process results in stripes with nonideal edges. Atomic force microscopy (AFM) topographical scans of the 700 nm stripe, Figs. 1(b), show that the edges have significant excess material and that opposite edges of the stripe have different geometries. These AFM scans were performed with a commercial, nonmagnetic tip.

During operation of the ferromagnetic-resonance force microscope, a dc magnetic field is applied in plane, along the waveguide axis and perpendicular to the sample stripe axis, aligning the magnetization of both the tip and sample along the field direction. This field configuration is varied slightly for angular-dependence measurements, described below. The microwave power supplied to the waveguide is modulated at the mechanical resonance frequency of the cantilever, providing an effective mechanical amplification of the magnetic tip sample forces. The amplitude of the cantilever oscillation provides the FMRFM signal that we describe below. Changes in the cantilever resonance frequency are tracked by a phase-locked loop, which also provides the power modulation signal.

To aid interpretation of the measurement results, we modeled the magnetization dynamics and tip sample interactions for a calculation of the net tip force due to magnetic excitations in the sample. For these calculations, we model the tip as a magnetically soft sphere, 500 nm in diameter, except as noted below. For each tip position $\mathbf{r}$, the dipolar tip field and the uniform applied field $H\hat{\mathbf{x}}$ are included in a calculation of the dynamic response $\mathbf{M}(\mathbf{r}',t|\mathbf{r})$ to a transverse driving field. The quasistatic change of the magnetization due to excitations is approximated by

$$\delta M_x(\mathbf{r}'|\mathbf{r}) \approx \frac{1}{2M_s} \langle M_y(\mathbf{r}',t|\mathbf{r})^2 + M_z(\mathbf{r}',t|\mathbf{r})^2 \rangle_t, \quad (1)$$

where $\langle\rangle_t$ indicates an average over a time scale that is long compared to the nanosecond precession time scale and short compared to the millisecond cantilever vibration time scale. The net change in tip force is then calculated by numerically integrating the dipolar forces between the sample magnetization change $\delta M_x(\mathbf{r}'|\mathbf{r})$ and the dipole moment of the tip. Details of the models are included in the Appendix.

III. RESULTS AND DISCUSSION

A. Spectroscopy

Figure 2 shows measured and modeled spectra for the 700 nm stripe. The excitation frequency is 8.0 GHz, and the spectra are obtained as a function of applied field for different tip positions, over the center of the stripe and over each of the edges. The tip is lifted 100 nm from contact with the sample surface. With the tip over the stripe center, the spectrum includes a strong positive peak with a high-field shoulder and two weaker peaks at higher field. With the sign convention used here, the positive signal indicates a repulsive static interaction between the tip and the static sample magnetization. In contrast to the tip-over-center spectra, with the tip positioned over the stripe edge, the highest-field mode is stronger and the lowest-field mode becomes weaker and changes sign. We label the strong, low-field modes as center modes and the weaker, high-field modes as edge modes. Justification for this labeling choice will be provided below.

The general features of the experimental and model spectra are similar for both the center and edge modes. The center mode is strongest and changes sign as the tip moves from center to edge. One significant difference is that the high-field edge mode in the modeled result occurs at a significantly higher field than the experimental result, a difference of roughly 200 mT. We attribute this large difference in resonance fields to the contrast between the nonideal edges of the sample and the perfectly smooth, vertical edges of the model. Previous studies[4,11,13,15] have attributed large differences between experimental and modeled edge resonance fields to a variety of possible edge defects.

The resonances are further characterized through the frequency dependence of the resonance fields. Frequency versus resonance field data sets, plotted in Fig. 3, were fit to the Kittel
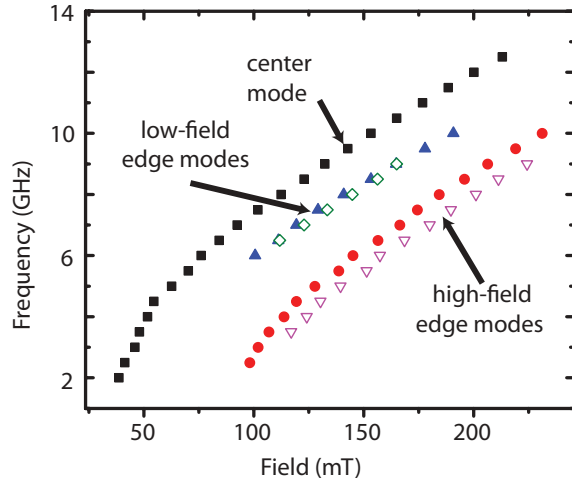
FIG. 3. (Color online) Experimental frequency vs field data for center mode, high-field edge modes, and low-field edge modes for the 700 nm stripe. Filled and open symbols correspond to the left and right edges, respectively. The external field is applied in plane, perpendicular to the long stripe axis.

FMR equation,

$$2\pi f(H) = \mu_0\gamma\sqrt{(H + H_1)(H + H_2)},\qquad(2)$$

to obtain the parameters shown in Table I. Here $f(H)$ is the FMR resonance frequency, H is the applied field at resonance, and H_1 and H_2 are fitting parameters where $-H_1$ is the saturation field, and H_2 is the effective out-of-plane anisotropy. Clear differences in the saturation field and effective out-of-plane anisotropy field are observed between the left and right edge modes. Similar fitting was used to obtain H_1 and H_2 parameters from modeled spectra. Differences between experimental and modeled edge mode H_1 values are especially prominent, as discussed above.

The dependence of the resonance fields on applied field orientation yields strong differences between the angular dependence of the edge modes and the center modes.[11] Figure 4 shows angular dependence of resonance fields at 8 GHz for the 700 nm stripe. The field orientation is rotated in the plane of the stripe, with the field oriented perpendicular to the stripe edge at 0 deg. The edge modes show a strong angular dependence around the perpendicular orientation, while the bulk mode, in contrast, shows only slight angular dependence. Experimental data largely follow the model's angular behavior, although with substantial differences between modeled and experimental edge mode resonance fields.

TABLE I. Experimental and modeled saturation field, $-H_1 = M_s$, and effective out-of-plane anisotropy, H_2, for the left, right, and center modes extracted from fitting to the Kittel FMR equation. Uncertainties are the standard deviations of the fit parameters.

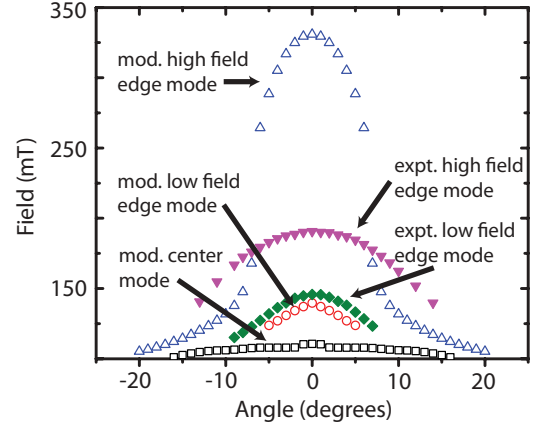| Mode	Experimental		Modeled	
	μ_0H_1 (mT)	μ_0H_2 (mT)	μ_0H_1 (mT)	μ_0H_2 (mT)
Left	-86.1 ± 0.8	462 ± 98	-193.69 ± 0.01	242.4 ± 0.3
Right	-91.6 ± 1.9	307 ± 99	-193.69 ± 0.01	242.4 ± 0.3
Center	-23 ± 1.8	584 ± 71	-19.56 ± 0.03	754.2 ± 0.5

FIG. 4. (Color online) Angular dependence of the different resonances for measured data (filled symbols) and modeled data (open symbols) for the 700 nm stripe. Edge modes have a prominent angular dependence.

B. Imaging

In the previous section, comparisons between the measured resonances and the modeled resonances of center modes and edge modes have supported our choice to label the lowest-field resonance as a center mode and the higher-field weaker resonances as edge modes. In this section we use the imaging capabilities of the microscope to clearly identify the edge modes and the center modes.

Figure 5 shows 1D spectroscopic scans across the stripes. For each point across the width of the stripes, the applied field is swept to yield spectra similar to those shown in Fig. 2, and the spectra are compiled into the images shown where the light color corresponds to a positive FMRFM signal. The excitation frequency is 8.1 GHz and the tip is lifted 100 nm off of the sample surface.

In Fig. 5, it is clear that the center modes and edge modes are detected near the center and edges of the stripe, respectively. The resonances near 120 mT are strongest when the tip is over the center of the stripe, and the higher-field resonances are strongest when the tip is located over the stripe edges. For the 700 nm stripe the bulk mode occurs in the middle of the stripe with a width that nearly covers the bulk of the stripe. Faint edge modes appear at fields just above the bulk mode, and a stronger set of edge modes appears around 200 mT with the left and right edge resonances separated by 17 mT; similar features are observed for the 400 nm stripe.

The images of the resonances in Fig. 5 have a characteristic arrowhead shape, and the results of two models (Fig. 6) show that this shape results from the tip field. In each model, the edge mode is perturbed by the tip field at the edge, which is a function of the tip position. When the tip is directly over the mode center the area beneath the tip is at a lower field since the tip field is antiparallel to the external field. Greater applied field is therefore needed to meet the resonance condition, so the resonance field is at a maximum. Moving the tip to either side of each mode center reduces the tip field at the mode center and thus the resonance field decreases. Additionally, the tip sample force changes from repulsive (when the tip is directly over the sample) to attractive (when the tip is to the
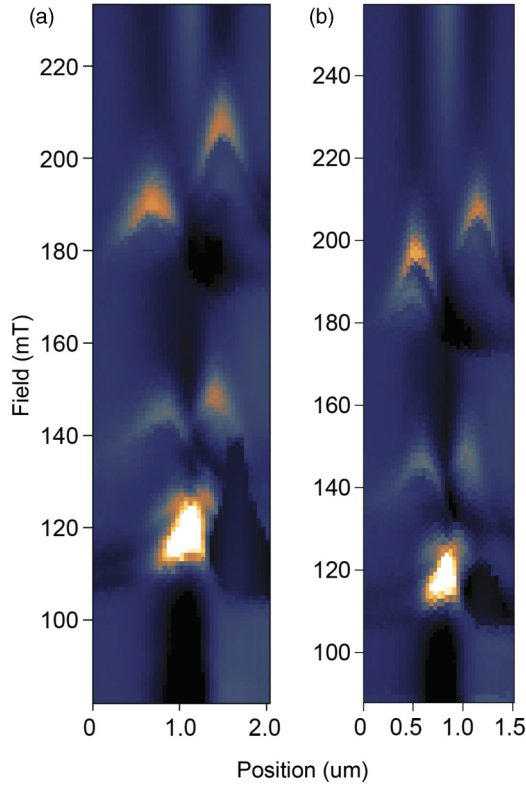
FIG. 5. (Color online) 1D FMRFM spectroscopic scans across the width of the stripes for (a) the 700 nm stripe and (b) the 400 nm stripe. Vertical line cuts correspond to spectra similar to those in Fig. 2. The bulk modes occur around 120 mT while the edge modes appear around 200 mT. The contrast has been stretched in each case to ensure visibility of the pseudoedge modes near 145 mT.

side) and the FMRFM signal consequently changes sign. The details of the models are provided in the Appendix.

Figure 6 shows two edge mode resonance models that differ in their assumptions regarding the profile of the edge mode. In the first column of Fig. 6, we assume that the edge mode profile is uniform along the stripe edge, as in the unperturbed case. The effective tip field is calculated as a weighted average of the tip field along the sample edge (A5), and this averaging has the effect of diluting the tip field, so that the maximum resonance shift is considerably less than the 20 mT maximum tip field.

The second column of Fig. 6 presents results of micromagnetic modeling of the edge mode resonance. Figure 6(b) shows the mode profile of the edge mode resonance, which is spontaneously localized under the tip. The full width at half maximum of the mode profile is 590 nm along the edge direction. The corresponding image of the edge mode resonance is shown in Fig. 6(d). In comparison to the analytical model, the maximum resonance shift is intermediate between the 20 mT maximum tip field experienced by the point-dipole macrospin and the spatially averaged field experienced by the uniform edge mode.

Using resonance fields from the 1D scans we performed 2D scans at the resonance field of each mode at a tip sample separation of 100 nm, Figs. 7(a)–7(f). Consider first the images of the 700 nm stripe [Figs. 7(a)–7(c)]. With the field set at
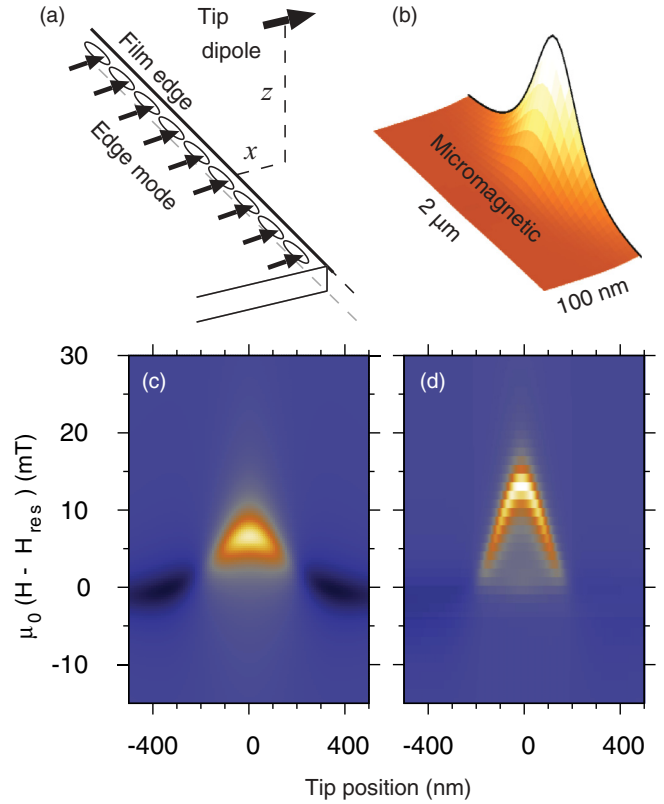

FIG. 6. (Color online) Model results for analytical and micromagnetic models of edge modes interacting with a point-dipole tip. The maximum tip field is 20 mT in each case. Panels (a) and (c) describe the analytical model, where the edge mode precession is assumed to occur uniformly along the edge of the stripe. Panels (b) and (d) describe the micromagnetic model results, where the edge mode precession is spontaneously localized under the tip, and the resonance is more strongly shifted by the tip field.

190 mT (the resonance field of the left edge) the left edge mode is clearly imaged in Fig. 7(a) while faint outlines are visible
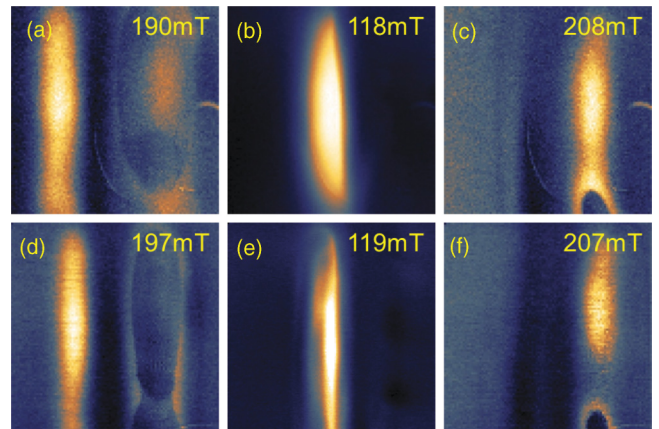

FIG. 7. (Color online) FMRFM scans of the stripes, $2\,\mu m \times 2\,\mu m$ with the external field fixed at the resonant fields of (a and d) the left edge mode, (b and e) the center mode, and (c and f) the right edge mode for the 700 nm stripe (top row) and 400 nm stripe (bottom row). The images are centered vertically on the $2\,\mu m$ center conductor of the waveguide.

surrounding the location of the right edge. We suggest that the origin of these outlines can be understood by considering a horizontal line cut through Fig. 5(a) at 190 mT. The line would not only intersect the center of the left edge mode but also the tails of the arrowhead-shaped right edge mode resonance. With the applied field set at 208 mT (the resonance field of the right edge), only the right edge mode is imaged. No outline of the left edge is observed since the right edge mode occurs at a higher field. When the field was set at 118 mT, only the center mode was observed.

Two-dimensional scans of the 400 nm stripe reveal effects that are similar to those found in the 700 nm stripe. The primary difference is that the center mode is roughly 300 nm in width owing to the smaller stripe width. The edge mode widths in the 400 nm stripe are similar in size. We note in passing that the edge mode images are less uniform along their lengths than the center mode images. Also, the images of the right edge modes appear to be less uniform than the images of the left edge modes in both stripes. We speculate that the difference in edge mode uniformity is associated with the structural asymmetry shown in the AFM image of Fig. 1(b), where the left edge has a continuous ribbon of excess material, while on the right edge the excess material is not continuous.

C. Resolution

A highly localized edge mode provides a small feature that appears to be convenient for investigating the spatial resolution of the FMRFM. Naively, one might expect that the edge mode resolution will be simply determined by the tip sample geometry alone, while the center mode will produce a broader image, owing to the larger extent of the center mode. In practice, we find that determining an estimate of resolution using the edge mode is more complicated.

As the tip moves along its path over the sample edge, there are several important effects to consider. One effect is that the field at the edge depends on the position of the tip. The tip field starts small and positive when the tip is distant, it grows, changes sign, and then goes through a minimum when the tip is directly over the edges. The resonance field goes through a corresponding maximum at this tip position. The profile of the edge mode also changes, from precession that is uniform along the edge, to a localized mode, and back to an extended edge mode. Additionally, the force on the tip due to the excitation changes sign as the tip approaches or moves away from the edge.

Figures 8(a) and 8(b) display tip scans across the center and left edge modes for different tip sample separations. The tip was set over the 700 nm stripe and scanned across the width of the stripe with the field set to the field for maximum signal for either the center mode [Fig. 8(a)] or the left edge mode [Fig. 8(b)]. Peak width values were extracted by fitting the peaks to Lorentzians. These values are plotted in Fig. 8(c). For tip lift heights greater than 200 nm, the image widths increased linearly with the lift height for both the center and edge modes. Below 200 nm, however, the image width reaches a minimum width on the order of 200 nm. For reasons that we do not fully understand, the center resonance width in this measurement is narrower than the edge mode, while in the 1D spectroscopic scans the center mode is wider. However, from the 1D images
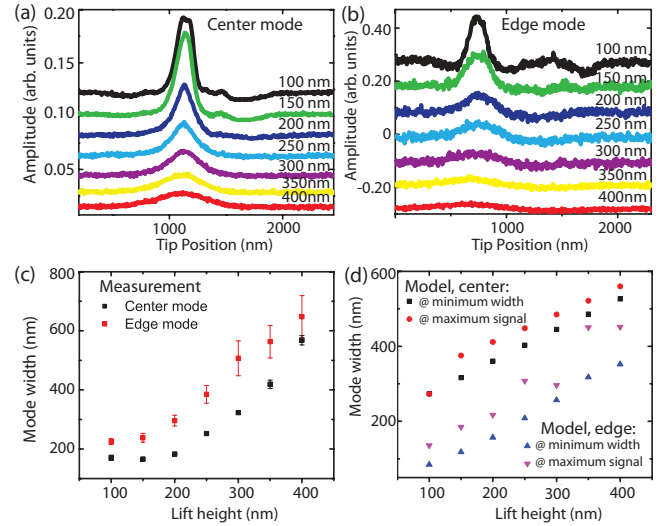

FIG. 8. (Color online) (a) Experimental 1D spatial scans across the width of the 700 nm stripe for various tip-sample separations with field set to the resonance of (a) the center mode and (b) the left edge mode. (c) Peak width for the center and left edge mode at various tip sample separations. (d) Modeled OOMMF data for the center and edge modes with the points labeled *maximum* taken at the maximum force and the points labeled *minimum* extracted at the minimum scan width.

of Fig. 5 and modeling results of Figs. 6(c) and 6(d), it is clear that the image shape depends sensitively on the choice of applied field. For example, if the applied field is slightly below resonance, the signal peak may broaden or split into the tails of the arrowhead shape.

In order to interpret the experimental data we use the micromagnetic model to calculate peak widths. We calculate the full width at half maximum of modeled 1D tip scans for frequencies near the experimental resonance frequency and we select two values for plotting in Fig. 8(d): the width at the frequency of the maximum tip force and the minimum width. In contrast to the measurements, the modeling yields edge mode widths that are consistently lower than the center mode widths. Both center mode widths and edge mode widths increase roughly linearly with lift height.

The modeling also indicates that the apparent resolution may depend sensitively on the choice of frequency and applied field. The minimum width is generally found at a slightly lower frequency (higher applied field) than the conditions for the maximum tip force. The maximum force occurs at a point where the width depends sensitively on the field and frequency. This point is very close to the condition where the arrowhead image of the resonance [see Fig. 6(d)] splits into two "tails." As a consequence of this sensitivity, the discrete frequencies of our Fourier transform method (see the Appendix) produce the scatter in the "maximum" points plotted in Fig. 8(d).

IV. CONCLUSION

This paper demonstrates ferromagnetic-resonance force microscopy of edge modes in transversely magnetized $Ni_{80}Fe_{20}$ stripes. Resonance spectra of the opposite edges of the stripes reveal an asymmetry with high quantitative

precision, and spatial scans reveal magnetic inhomogeneity along each of the stripe edges. Micromagnetic modeling of the edge mode dynamics indicates that the stray field from the tip causes localization of the edge mode along the edge.

APPENDIX

As an aid to interpretation of the measurement results, we have used both analytical and micromagnetic modeling to describe the perturbation of the sample by the tip, the dynamics of the sample, and the forces exerted on the tip by the sample. In this Appendix, we describe the mathematical and computational details of the modeling.

The presence of a magnetic tip at position $\mathbf{r}$ on the cantilever produces a field at location $\mathbf{r}'$ in the sample. For simplicity, we assume that the tip behaves like a point dipole and the tip field is

$$H^{\text{tip}}(\mathbf{r},\mathbf{r}') = \frac{m_x^{\text{tip}}}{4\pi} \frac{3(x'-x)^2 - |\mathbf{R}|^2}{|\mathbf{R}|^5}, \quad (A1)$$

with the definition $\mathbf{R} \equiv \mathbf{r}' - \mathbf{r}$.

The tip field can have several effects on the magnetic resonances in the sample, including shifting the resonance field by an amount $H^{\text{eff}}(\mathbf{r})$, or it may have more profound effects, including modification of mode profiles or creation of localized modes.[21–25] These effects of the tip field on the sample add a layer of complication to the interpretation of FMRFM images, but the tip field can be included easily in calculations of the FMRFM response.

To calculate the sample dynamics, we consider only the linear case where the precessing components of the magnetization are small, and a susceptibility tensor $\chi(\mathbf{r}')$ describes the linear response of the magnetization at location $\mathbf{r}'$ to a uniform pumping field $H^{\text{pump}} e^{-i\omega t}$:

$$\begin{bmatrix} M_y(\mathbf{r}'|\mathbf{r}) \\ M_z(\mathbf{r}'|\mathbf{r}) \end{bmatrix} = \begin{bmatrix} \chi_{yy}(\mathbf{r}'|\mathbf{r}) & \chi_{yz}(\mathbf{r}'|\mathbf{r}) \\ \chi_{zy}(\mathbf{r}'|\mathbf{r}) & \chi_{zz}(\mathbf{r}'|\mathbf{r}) \end{bmatrix} \begin{bmatrix} H^{\text{pump}} \\ 0 \end{bmatrix}. \quad (A2)$$

Here we have adopted a coordinate system where the sample lies in the x-y plane and the applied field and sample magnetization are in the x direction. To lowest order, the resulting change in the x component of the magnetization is then given by Eq. (1):

$$\Delta \mathbf{M}_x(\mathbf{r}') \approx -\frac{|\chi_{yy}(\mathbf{r}')|^2 + |\chi_{zy}(\mathbf{r}')|^2}{4M_s} (H^{\text{pump}})^2. \quad (A3)$$

A change in the force between the tip and sample accompanies the precession when magnetic resonances are excited in the sample. Because the precession occurs at GHz-scale frequencies, and the cantilever responds only at kHz-scale frequencies, we consider only the quasistatic, longitudinal magnetization change and not the precessing components of the magnetization when computing the forces on the tip. The

tip force due to precession in the sample is given by integrating the dipole-dipole forces over the volume of the sample:

$$\delta F^{\text{tip}}(\mathbf{r}) \int_S d^3\mathbf{r}' \frac{3m^{\text{tip}} z(|\mathbf{R}|^2 - 5(x-x')^2)}{4\pi |\mathbf{R}|^7} \Delta M_x(\mathbf{r}'). \quad (A4)$$

Here, we have made the simplifying assumption that the tip moment and the magnetization change in the sample are all parallel to the applied field in the x direction.

The models considered here have the tip field given by Eq. (A1), the magnetization modulation given by Eq. (A3), and the tip force given by Eq. (A4) in common, but they differ in how these relations are evaluated. The following subsections describe the evaluation of these for a weak-interaction analytical model and for micromagnetic modeling of the FMRFM signal.

1. Weak interaction

In the weak-interaction limit, we calculate the tip sample forces using a perturbation approach to first order in the tip field. In this approximation, the profiles of the stripe's precession modes are unaffected by the presence of the tip field but the tip field does produce a first-order shift of the modes' respective resonance fields given by[21]

$$\delta H^{\text{eff}}(\mathbf{r}) \approx -\frac{\int_S d^3\mathbf{r}' \, p(\mathbf{r}')^2 \, H^{\text{tip}}(\mathbf{r},\mathbf{r}')}{\int_S d^3\mathbf{r}' \, p_i(\mathbf{r}')^2}. \quad (A5)$$

The integrals are carried out over the sample volume S and $p(\mathbf{r}')$ is the eigenmode's precession profile in the sample.

In the case of the edge mode, we recognize that the mode profile is concentrated within approximately 30 nm of the edge in a film with 25 nm thickness.[11] Since these distances are much smaller than the minimum distance to the tip (≈ 250 nm), we approximate the edge mode profile as precession only along a line at the sample edge:

$$p_{\text{edge}}(\mathbf{r}')^2 \propto \delta(x')\delta(z'). \quad (A6)$$

For an infinitely long edge, the effective tip field given by Eq. (A5) with this profile yields zero. The integral in the numerator is finite, but the denominator is the edge length. To describe our experiments, however, it seems reasonable to limit the edge mode length to the width, $W = 2 \ \mu$m, of the waveguide center conductor. Because the magnetic stripe is fabricated over the edges of the much thicker waveguide, the magnetic stripe will naturally bend at the edge of the waveguide as illustrated in Fig. 1(a). For this finite-length edge, the tip field shifts the edge mode resonance by

$$\delta H^{\text{eff}} = \frac{m_x^{\text{tip}} W(8x^4 + x^2 W^2 + 4x^2 z^2 - z^2 W^2 + 4z^4)}{2\pi(x^2 + z^2)^2(4x^2 + W^2 + 4z^2)^{3/2}}. \quad (A7)$$

Incorporating this tip-induced field shift estimate, the susceptibility has the form of a Lorentzian, centered at $H = H^{\text{res}} - \delta H^{\text{eff}}$:

$$|\chi(H,\mathbf{r}'|\mathbf{r})|^2 \propto \frac{p_{\text{edge}}(\mathbf{r}')^2}{[H - H^{\text{res}} + \delta H^{\text{eff}}(\mathbf{r})]^2 + \Delta H^2/4}. \quad (A8)$$

Here H is the applied field, H^{res} is the resonance field of the sample in the absence of the tip, and ΔH is the field-swept line width of the sample resonance.

With a model for the susceptibility in hand, we turn next to the calculation of the tip force. As with the calculation of the field shift, we use Eq. (A6) for the mode profile concentrated at the film edge. The tip force is proportional to

$$
\begin{aligned}
F(\mathbf{r}, H) \propto\ & m_x^{\text{tip}} W z [96 x^6 + 6 x^4 (5 W^2 + 28 z^2) \\
& - z^2 (W^4 + 10 W^2 z^2 + 24 z^4) \\
& + x^2 (3 W^4 + 20 W^2 z^2 + 48 z^4)] \\
& \times (x^2 + z^2)^{-3} \times (4 x^2 + W^2 + 4 z^2)^{-5/2} \\
& \times \{[H - H^{\text{res}} + \delta H^{\text{eff}}(\mathbf{r})]^2 + \Delta H^2/4\}^{-1}. \quad \text{(A9)}
\end{aligned}
$$

The first four lines of this expression describe the tip force due to a line segment of dipole "charge" that forms when the edge mode is excited. The final term describes the field dependence of the edge mode excitation amplitude, including the field shift $\delta H^{\text{eff}}(\mathbf{r})$ with its tip position dependence given by Eq. (A7).

Figure 6(c) shows the 1D spectral image generated by this analytical model. The tip moment was fixed at 9.5×10^{-15} Am^2 to yield a maximum tip field of $\mu_0 H^{\text{tip}} = 20$ mT and the line width was set at $\mu_0 \Delta H = 4.8$ mT.

2. Micromagnetic model

The modeled spectra were generated using the object oriented micromagnetic framework (OOMMF),[27] using a value of $\mu_0 M_s = 0.81$ T determined from fitting of the center

mode resonances in Fig. 3 and other parameters representative of Ni$_{80}$Fe$_{20}$ (exchange stiffness $A = 13$ pJ/m, $K_u = 0$). Sample geometry assumed perfectly rectangular edges on the stripe (thickness 25 nm and width 1000 nm), and the applied field included both a uniform component and a dipolar component from a point-dipole tip magnet. The tip moment was fixed at 9.5×10^{-15} Am^2 to yield a maximum tip field of $\mu_0 H^{\text{tip}} = 20$ mT.

The micromagnetic model is centered around a calculation of $\chi(\mathbf{r}')$. Starting from an equilibrium magnetization state, a short (0.1 ps), strong (1 T), uniform field pulse H^{pulse} provides broadband excitation that initially rotates the spins by approximately 1 deg. The relaxation of the magnetization is then calculated using the Landau-Lifshitz equations of motion and recorded at 512 time intervals of 20 ps. The resulting data set, $\mathbf{M}(\mathbf{r}', t)$, is Fourier transformed in time to yield magnetization profiles $\mathbf{M}(\mathbf{r}', \omega)$. Division by the Fourier transform of the field pulse yields the susceptibility tensor components, for example,

$$
\chi_{zy}(\omega, H, \mathbf{r}') = \frac{M_z(\mathbf{r}', \omega)}{H_y^{\text{pulse}}(\omega)}. \quad \text{(A10)}
$$

The tip force is then calculated using Eq. (A8) and numerical integration of Eq. (A4). Results are shown in Fig. 2 as spectra of tip force as a function of applied field and in Fig. 6(d) as a 1D spectral image.

*Current address: Everspin Technologies, Inc., Chandler AZ, USA.
†robert.mcmichael@nist.gov

[1] S. S. P. Parkin, M. Hayashi, and L. Thomas, Science **320**, 190 (2008).

[2] D. A. Allwood, G. Xiong, C. C. Faulkner, D. Atkinson, D. Petit, and R. P. Cowburn, Science **309**, 1688 (2005).

[3] S. A. Wolf, J. Lu, M. R. Stan, E. Chen, and D. M. Treger, Proc. IEEE **98**, 2155 (2010).

[4] M. Bailleul, D. Olligs, and C. Fermon, Phys. Rev. Lett. **91**, 137204 (2003).

[5] B. B. Maranville, R. D. McMichael, S. A. Kim, W. L. Johnson, C. A. Ross, and J. Y. Cheng, J. Appl. Phys. **99**, 08C703 (2006).

[6] J. Jorzick, S. O. Demokritov, B. Hillebrands, M. Bailleul, C. Fermon, K. Y. Guslienko, A. N. Slavin, D. V. Berkov, and N. L. Gorn, Phys. Rev. Lett. **88**, 047204 (2002).

[7] C. Bayer, S. O. Demokritov, B. Hillebrands, and A. N. Slavin, Appl. Phys. Lett. **82**, 607 (2003).

[8] J. P. Park, P. Eames, D. M. Engebretson, J. Berezovsky, and P. A. Crowell, Phys. Rev. Lett. **89**, 277201 (2002).

[9] C. Bayer, J. P. Park, H. Wang, M. Yan, C. E. Campbell, and P. A. Crowell, Phys. Rev. B **69**, 134401 (2004).

[10] V. V. Kruglyak, P. S. Keatley, R. J. Hicken, J. R. Childress, and J. A. Katine, J. Appl. Phys. **99**, 08F306 (2006).

[11] R. D. McMichael and B. B. Maranville, Phys. Rev. B **74**, 024424 (2006).

[12] R. D. McMichael, C. A. Ross, and V. P. Chuang, J. Appl. Phys. **103**, 07C505 (2008).

[13] M. Zhu and R. D. McMichael, J. Appl. Phys. **107**, 103908 (2010).

[14] M. Zhu and R. D. McMichael, J. Appl. Phys. **109**, 043904 (2011).

[15] B. B. Maranville, R. D. McMichael, and D. W. Abraham, Appl. Phys. Lett. **90**, 232504 (2007).

[16] R. Meckenstock, I. Barsukov, O. Posth, J. Lindner, A. Butko, and D. Spoddig, Appl. Phys. Lett. **91**, 142507 (2007).

[17] Z. Zhang, P. C. Hammel, and P. E. Wigen, Appl. Phys. Lett. **68**, 2005 (1996).

[18] O. Klein, G. de Loubens, V. V. Naletov, F. Boust, T. Guillet, H. Hurdequint, A. Leksikov, A. N. Slavin, V. S. Tiberkevich, and N. Vukadinovic, Phys. Rev. B **78**, 144410 (2008).

[19] P. C. Hammel and D. V. Pelekhov, in *Handbook of Magnetism and Advanced Magnetic Materials* (Wiley, New York, 2007), Vol. 5.

[20] Y. Obukhov, D. V. Pelekhov, E. Nazaretski, R. Movshovich, and P. C. Hammel, Appl. Phys. Lett. **94**, 172508 (2009).

[21] Y. Obukhov *et al.*, Phys. Rev. Lett. **100**, 197601 (2008).

[22] E. Nazaretski, D. V. Pelekhov, I. Martin, M. Zalalutdinov, D. Ponarin, A. Smirnov, P. C. Hammel, and R. Movshovich, Phys. Rev. B **79**, 132401 (2009).

[23] I. Lee, Y. Obukhov, G. Xiang, A. Hauser, F. Yang, P. Banerjee, D. Pelekhov, and P. Hammel, Nature (London) **466**, 845 (2010).

[24] I. Lee, Y. Obukhov, A. J. Hauser, F. Y. Yang, D. V. Pelekhov, and P. C. Hammel, J. Appl. Phys. **109**, 07D313 (2011).

[25] H.-J. Chia, F. Guo, L. M. Belova, and R. D. McMichael, Phys. Rev. Lett. **108**, 087206 (2012).

[26] L. M. Belova, E. D. Dahlberg, A. Riazanova, J. J. L. Mulders, C. Christophersen, and J. Eckert, Nanotechnology **22**, 145305 (2011).

[27] M. J. Donahue and D. G. Porter, in *Interagency Report NISTIR 6376* (National Institute of Standards and Technology, Gaithersburg, 1999).